Nanoscale Research Letters

NANO EXPRESS Open Access

A Monoclinic $V_{1-x-y}Ti_xRu_yO_2$ Thin Film with Enhanced Thermal-Sensitive Performance

Yatao Li, Deen Gu*, Shiyang Xu, Xin Zhou, Kai Yuan and Yadong Jiang

Abstract

Preparing the thermal-sensitive thin films with high temperature coefficient of resistance (TCR) and low resistivity by a highly compatible process is favorable for increasing the sensitivity of microbolometers with small pixels. Here, we report an effective and process-compatible approach for preparing $V_{1-x-y}Ti_xRu_yO_2$ thermal-sensitive thin films with monoclinic structure, high TCR, and low resistivity through a reactive sputtering process followed by annealing in oxygen atmosphere at 400 °C. X-ray photoelectron spectroscopy demonstrates that Ti^{4+} and Ru^{4+} ions are combined into VO_2. X-ray diffraction, Raman spectroscopy, and transmission electron microscopy reveal that $V_{1-x-y}Ti_xRu_yO_2$ thin films have a monoclinic lattice structure as undoped VO_2. But $V_{1-x-y}Ti_xRu_yO_2$ thin films exhibit no-SMT feature from room temperature (RT) to 106 °C due to the pinning effect of high-concentration Ti in monoclinic lattice. Moreover, RT resistivity of the $V_{0.8163}Ti_{0.165}Ru_{0.0187}O_2$ thin film is only one-eighth of undoped VO_2 thin film, and its TCR is as high as 3.47%/°C.

Keywords: Vanadium oxide, Thin films, Titanium, Ruthenium, Thermal-sensitive

Introduction

Microbolometers have been widely applied in civil and military fields. One of the important development trends is reducing the pixel size in order to reduce product cost and increase the detection range [1]. However, the miniaturization causes the decrease of sensitivity. Improving the micro-electromechanical system (MEMS) manufacturing process to optimize the filling factor, absorption coefficient, thermal conductivity, and other key factors can effectively enhance the sensitivity, but this approach is coming to its limit [1]. Another effective way is using better thermal-sensitive materials [2]. As a widely used thermal-sensitive material, VO_x with a relatively low resistivity in the range of 0.1–5.0 Ω·cm has a TCR of about 2%/°C at room temperature [3]. Considering that the sensitivity of a microbolometer is proportional to the TCR, it is more favorable to use thermal-sensitive materials with higher TCR for increasing the sensitivity of small pixel microbolometers. In order to increase the TCR of VO_x films, Jin et al. prepared Mo-doped VO_x thin films by bias target ion beam deposition [3]. The films have a high TCR of − 4.5%/°C, but large resistivity (> 1000 Ω·cm) is not preferable for microbolometer applications.

For fabricating a typical VO_x-based bolometer array, it is necessary to cover VO_x thermal-sensitive thin film with a passivation layer (SiN_x or SiO_x), which can protect the thermal-sensitive thin film from the oxidation by subsequent processes (removing of photoresist, release of sacrificial layer, etc.) [4]. The protection effect of the passivation layer depends on its film density. Denser passivation layer results in better protection effect. Generally, high preparation temperature contributes to denser passivation layer [5, 6], thus better protection effect for VO_x thin films. However, VO_x thermal-sensitive thin films, which are generally prepared at relatively low temperature (lower than 300 °C), are amorphous [3, 7, 8]. Whereas amorphous VO_x tends to crystallize at elevated temperature [9]. Once the crystallization happens, electrical parameters of the film will be significantly changed. Therefore, relatively low preparation temperature for VO_x thermal-sensitive thin films constrains the process

* Correspondence: gudeen@163.com
School of Optoelectronic Science and Engineering, University of Electronic Science and Technology of China, Chengdu 610054, Sichuan, People's Republic of China

for the passivation protection layer. This causes an annoying problem for fabricating bolometer arrays: the very stringent control on the subsequent processes.

Monoclinic vanadium dioxide (VO_2) thin films have been considered as a potential thermal-sensitive material for highly sensitive microbolometers owing to high TCR at room temperature (RT). Moreover, monoclinic VO_2 thin films are prepared at higher temperature than 300 °C [10], which is beneficial for preparing denser passivation protection layer at higher temperature. However, the two characteristics of monoclinic VO_2 limit, to a certain extent, its practical application for microbolometers. On the one hand, the semiconductor-to-metal transition (SMT) happens to VO_2 near about 68 °C. The hysteretic feature and strain changes during the SMT of VO_2 will deteriorate the device performance and reduce the reliability of the device [11]. On the other hand, relatively high RT resistivity (> 10 Ω·cm) restricts the choice of device operating parameters [12, 13]. Therefore, preparing the vanadium dioxide films with high TCR, non-SMT, low resistivity, and crystallization structure becomes a challenge for developing high-performance thermal-sensitive materials for microbolometers. Recently, Soltani et al. introduced both Ti and W into VO_2 thin films in order to suppress the SMT [14], and prepared Ti-W co-doped VO_2 thin films with non-SMT feature and a high TCR. However, Ti-W co-doped VO_2 thin films have a similar resistivity to undoped VO_2.

In this article, we demonstrate a high-performance monoclinic $V_{1-x-y}Ti_xRu_yO_2$ thermal-sensitive thin film through a SMT-inhibition strategy by means of introducing Ti and Ru ions into VO_2 thin films. The thin films were prepared by a reactive sputtering process followed by annealing at 400 °C. Higher process temperature than amorphous VO_x thin films provides more parameter choice of subsequent MEMS processes for bolometer devices. $V_{1-x-y}Ti_xRu_yO_2$ thin films have similar monoclinic structure to undoped VO_2, but the SMT feature is completely suppressed due to the pinning effect of high-concentration dopants. The thin film with optimal dopant concentration has higher TCR (3.47%/°C) than the commercial VO_x thin films, and much lower RT resistivity than undoped monoclinic VO_2 thin films.

Material and Methods

All the thin films were prepared through direct current (DC) reactive magnetron sputtering on quartz substrates (23 mm × 23 mm × 1 mm). A high-purity vanadium target (99.99%) with a diameter of 80 mm and a thickness of 4 mm was used for depositing thin films with a target-substrate distance of about 11.5 cm. After the base pressure is below 2.0×10^{-3} Pa, the sputtering was executed at 0.32A with an O_2/Ar ratio of 1:50. During deposition, the substrate temperature was kept at 100 °C. Then as-deposited thin films were in situ annealed for 60 min at 400 °C in pure oxygen (4.4 sccm). The thickness of films was controlled as about 380 nm according to the calibrated deposition rate. Ti and Ru were introduced with pure Ti pieces (99.9% purity, 10 mm × 10 mm × 2 mm) and V/Ru alloy pieces (consisting of 10.0 at.% Ru and 90.0 at.% V, 10 mm × 10 mm × 2 mm) placed symmetrically on the sputtered surface of the V target. $V_{1-x-y}Ti_xRu_yO_2$ thin films using 3 Ti pieces and 1, 2, 3 V/Ru alloy piece(s), Ti-doped thin film using 3 Ti pieces, and undoped VO_2 thin film are marked as VTRO-1, VTRO-2, VTRO-3, VTO, VO, respectively.

The chemical states of dopants (Ti and Ru) were analyzed by X-ray photoelectron spectroscopy (XPS) with Al Kα radiation (1486.6 eV) using a ESCALAB 250 (Thermo instrument). The binding energies (BEs) were calibrated to the C 1 s peak at 284.6 eV from the adventitious carbon. The concentrations of dopants in $V_{1-x-y}Ti_xRu_yO_2$ thin films were checked by energy dispersive X-ray spectroscopy (EDS). The crystalline structure of the films was examined by X-ray diffraction (XRD) on a Bruke D8 diffractometer (Cu Kα irradiation) and transmission electron microscopy (TEM) on Titan G2 60–300. Raman spectra were characterized by means of a confocal α-Raman spectrometer with the excitation wavelength of 514 nm and an irradiation power of about 0.5 mW (Renishaw inVia). The surface morphology of samples was observed by scanning electron microscopy (SEM, SU8020, Hitachi). The temperature-dependent resistivity of thin films was obtained at a temperature interval of 2 °C according to the thickness and sheet resistance, which was recorded using a four-point probe (SX1934) along with a heating plate.

Results and Discussion

The chemical states of dopants in the films were determined by XPS analyses. Figure 1 a shows the XPS survey spectra of VO, VTO, and VTRO-3, clearly showing the strong peaks of V2p, O1s, Ti2p, and C1s. The peak of Ru 3d in $V_{1-x-y}Ti_xRu_yO_2$ thin films as a shoulder signal of about 281.4 eV can be observed near the C 1 s peak [15]. The successful incorporation of Ti^{4+} and Ru^{4+} ions into the VO_2 lattice is demonstrated by the Ti 2p peak and the Ru 3d peak of VRTO-3 in Fig. 1 b and c. The Ti $2p_{1/2}$ peak at 464.0 eV, the Ti $2p_{3/2}$ peak at 458.3 eV, and splitting energy of 5.7 eV for the Ti 2p doublet indicate the oxidation state of Ti^{4+} ions in VTO and VTRO-3 [16]. Figure 1 c exhibits the Ru 3d XPS spectrum for VTRO-3. The binding energy of 281.4 eV suggests the presence of Ru^{4+} ions in VTRO-3 [16]. The presence of Ti and Ru elements can be further verified by EDS analysis as shown in Fig. 1f. The doping concentrations of Ti and Ru elements (x, y in $V_{1-x-y}Ti_xRu_yO_2$), obtained by EDS analyses, for all the samples are listed in Table 1.

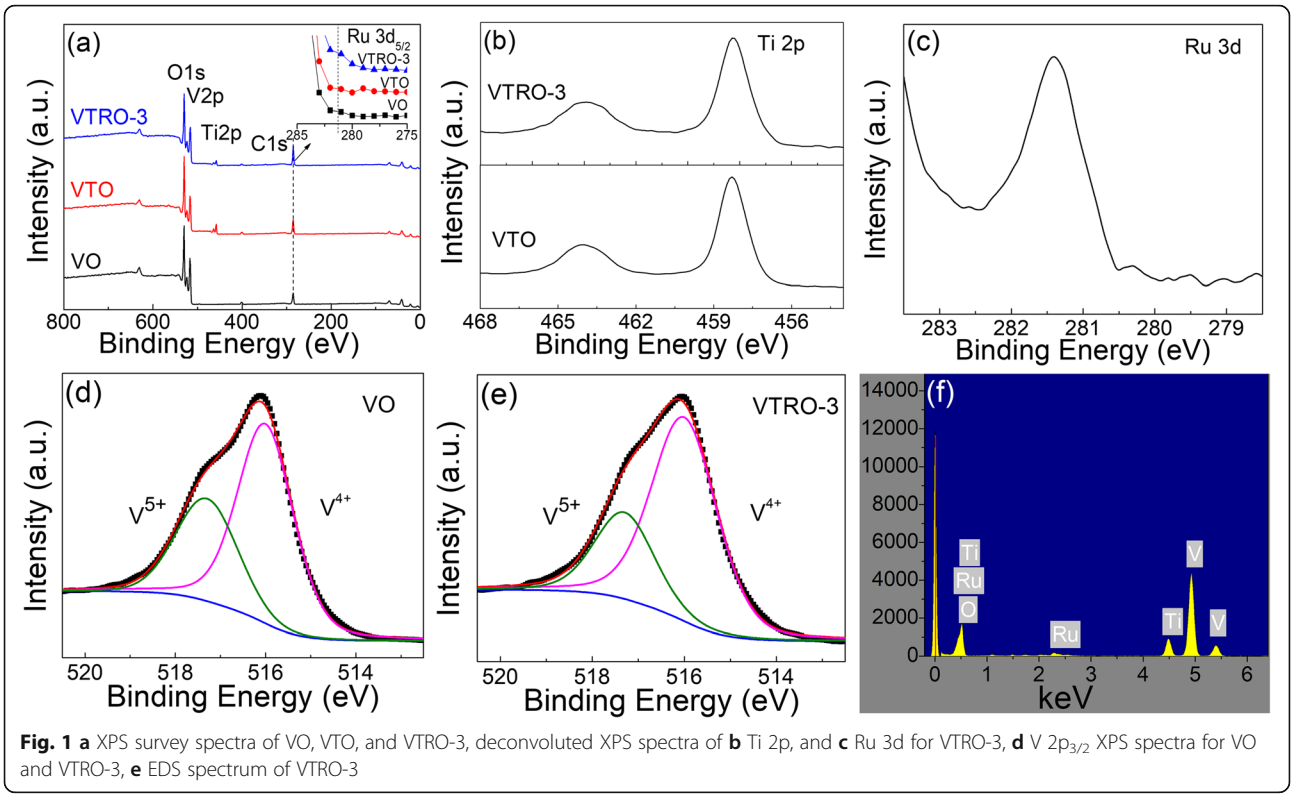

Fig. 1 **a** XPS survey spectra of VO, VTO, and VTRO-3, deconvoluted XPS spectra of **b** Ti 2p, and **c** Ru 3d for VTRO-3, **d** V $2p_{3/2}$ XPS spectra for VO and VTRO-3, **e** EDS spectrum of VTRO-3

High-concentration Ti was introduced into $V_{1-x-y}Ti_xRu_yO_2$ thin films. The doping level of Ru in the thin films was well controlled by varying the number of V/Ru alloy pieces.

Moreover, the oxidation states of vanadium ions in films were also analyzed from the deconvoluted V $2p_{3/2}$ peaks using the Shirley function [17–19]. Figure 1 d and e shows the high-resolution V $2p_{3/2}$ XPS spectra for VO and VTRO-3. The V 2p spectra both consist of two peaks at 517.4 eV, indicative of V^{5+}, and 516.1 eV, indicative of V^{4+} [20]. The appearance of V^{5+} ions could be ascribed to natural oxidation of the sample surface during storage in the air [21, 22]. Specifically, the relative contents of V^{5+} species in VO and VTRO-3, estimated from the integrated intensity of V 2p peak shown in Fig. 1 d and e, are 34.5% and 28.0%, respectively. The relative contents of V^{4+} species in VO and VTRO-3 are 65.5% and 72.0%, respectively.

Table 1 Doping levels of Ti and Ru, crystallite size, resistivity, and TCR of all the samples

Sample no.	VO	VTO	VTRO-1	VTRO-2	VTRO-3
Ti concentration (x, %)	–	17.6	17.1	16.7	16.5
Ru concentration (y, %)	–	–	0.65	1.36	1.87
Crystallite size (nm)	25.5	27.6	24.7	17.2	12.5
Resistivity (at 26 °C, Ω·cm)	13.5	12.8	6.53	3.14	1.55
TCR (%/°C)	− 3.13	− 3.46	− 3.54	− 3.46	− 3.47

This indicates that $V_{1-x-y}Ti_xRu_yO_2$ thin film shows higher stability than undoped VO_2.

To confirm the crystalline structures, XRD patterns of all the samples were collected (Fig. 2a). All the films exhibit monoclinic structure of VO_2 (PDF No. 43-1051) [23]. For all the films, the (011) peak seems to be of higher intensity than the other peaks, revealing a preferential growth along (011) facet. No diffraction peaks from other vanadium oxide (V_2O_3, V_2O_5) [22] or titanium/ruthenium oxide phases can be detected [24]. Also, it is worth noting that V^{5+} ions are probed by XPS while there are no characteristic peaks of the V_2O_5 phase in XRD patterns. Considering that XPS is a surface-sensitive technique and the XRD analysis reveals the lattice structure of the whole sample, the presence of V^{5+} ions is believed to be derived from surface oxidation during storage and it exists only on the surface of samples as reported previously [24–27] .

Figure 2 b further shows the close-up views of (011) peak for all the samples after fitting with Lorentzian function. Compared to VO, the (011) diffraction peak of VTO moves from 27.78 to 27.76°. This implies Ti-doping causes a slight increase of the interplanar spacing of (011) facet due to the substitutional presence of Ti in monoclinic VO_2 [28, 29]. As for $V_{1-x-y}Ti_xRu_yO_2$, the peak position of the (011) facet shift toward a larger angle (from 27.78° for VO to 27.86° for VTRO-2), indicating that the interplanar lattice spacing varies along

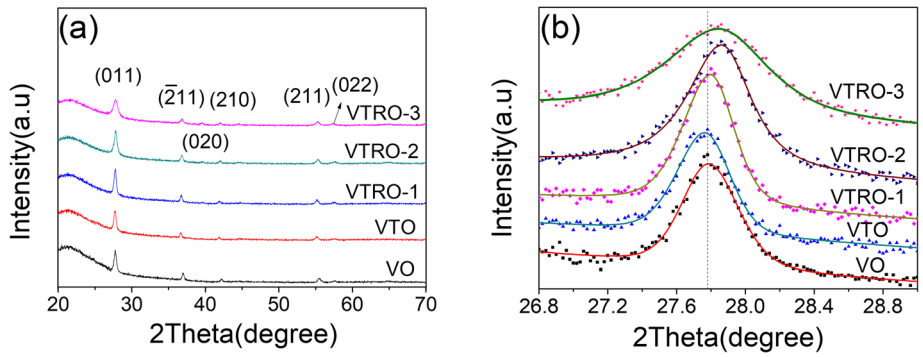

Fig. 2 **a** XRD patterns and **b** close-up views of (011) peaks of all the samples

(011) facet. This should originate from the replacement of some V^{4+} ions in the monoclinic lattice by Ru^{4+} with a larger ionic radius. According to the Scherrer's formula, the average crystallite size was estimated from the diffraction data of (011) facet by the Scherrer equation [30]. VTO has larger crystallite size than VO (Table 1). This reveals that Ti-doping promotes the growth of VO_2 crystallites. But the addition of Ru reduces the crystallite size of films. With increasing the concentration of Ru, $V_{1-x-y}Ti_xRu_yO_2$ thin films (VTRO-1, VTRO-2, VTRO-3) exhibit gradually reduced crystallite size. Our previous work has demonstrated that Ru^{4+} ions in the VO_2 lattice inhibit the growth of VO_2 crystallites in Ru-doped VO_2 thin films [24]. Similarly, the Ru^{4+} ions suppress the coalescence of adjacent crystallites in $V_{1-x-y}Ti_xRu_yO_2$ thin films, thus decrease the crystallite size of films.

The direct observation of the monoclinic lattice in VO and VTRO-3 was performed by means of TEM analysis [31–33]. Figure 3 a and b shows the selective area diffraction (SAD) patterns of VO and VRTO-3. They exhibit clear series of Debye-Scherrer diffraction rings, which can be indexed as monoclinic VO_2. This suggests the monoclinic polycrystalline feature of undoped VO_2 and $V_{1-x-y}Ti_xRu_yO_2$ thin films, which is accordant with the XRD analyses. The high-resolution TEM (HRTEM) images shown in Fig. 3 c and d reveal the clear lattice fringes from monoclinic VO_2. This further demonstrates that $V_{1-x-y}Ti_xRu_yO_2$ thin films have the monoclinic

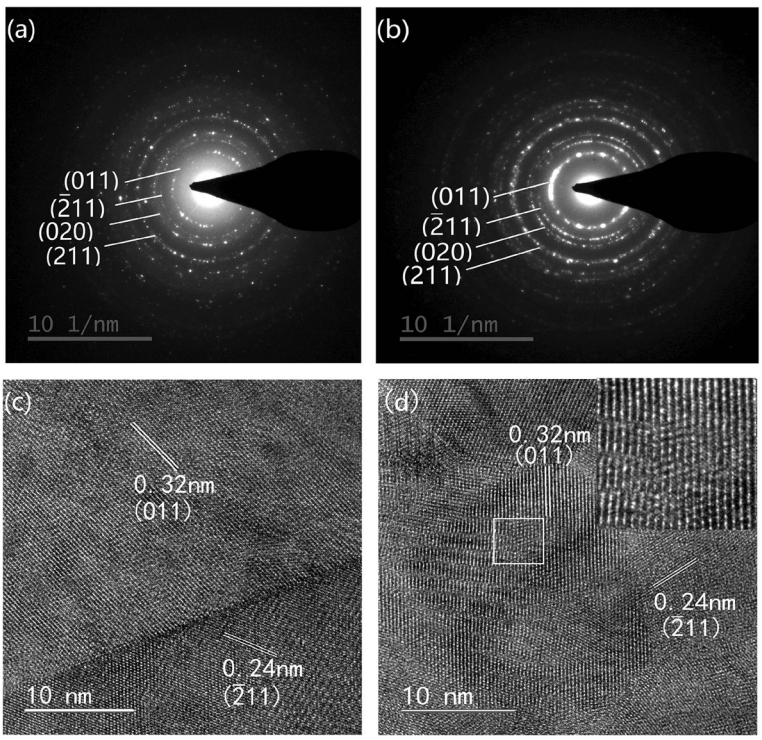

Fig. 3 **a** and **b** SAD patterns, **c** and **d** HRTEM images of VO and VTRO-3

structure as the undoped one (VO) [34]. But the insert in Fig. 3d shows the distortion of local lattice fringes in a crystallite of VTRO-3. This indicates that the introduction of Ti and Ru dopants causes obvious disturbance in the lattice of monoclinic VO_2.

Figure 4 shows the Raman spectra obtained at RT for the films. All the Raman peaks for VO can be attributed to the A_g and B_g phonon modes from the monoclinic VO_2 [35]. No Raman modes from V_2O_5 can be observed [24]. Three prominent Raman modes (ω_1 around 193 cm^{-1}, ω_2 around 223 cm^{-1}, and ω_3 around 613 cm^{-1}) are used for further probing the influence of the doping on the crystalline structure of VO_2 thin films. Ti-doped VO_2 thin film (VTO) has the similar high-frequency phonon mode (ω_3) as VO_2 (VO), typical of monoclinic VO_2. Differently, two low-frequency modes (ω_1 and ω_2) in VTO exhibit obvious redshift compared with undoped VO_2. The low-frequency modes ω_1 and ω_2 can be ascribed to the V-V vibrations [36]. The redshift of ω_1 and ω_2 indicates Ti^{4+} ions was introduced into the zigzag V-V chains in monoclinic VO_2 [37], which decreases the Raman frequencies of the V-V vibrations due to the local structure perturbations around Ti^{4+} ions.

The high-frequency phonon mode ω_3 is still observed for $V_{1-x-y}Ti_xRu_yO_2$ thin films, which suggests the presence of monoclinic VO_2. This is consistent with the XRD and TEM analyses. But their Raman intensities of ω_3 outstandingly decrease compared with VO and VTO. The other Raman peaks remarkably weaken, even disappear with increasing the Ru concentration. This indicates that there is local disturbance in monoclinic VO_2 lattice due to the existence of Ti and Ru ions. The previous work has demonstrated that the Ru^{4+} ions in the VO_2 lattice conduce to inducing the local tetragonal symmetry in the monoclinic framework since the Ru–O coordination exhibits an almost identical symmetry to tetragonal VO_2 [24, 38]. The tetragonal symmetry has lower Raman activity than the monoclinic phase [39]. Thus, the $V_{1-x-y}Ti_xRu_yO_2$ thin films show much lower Raman intensity.

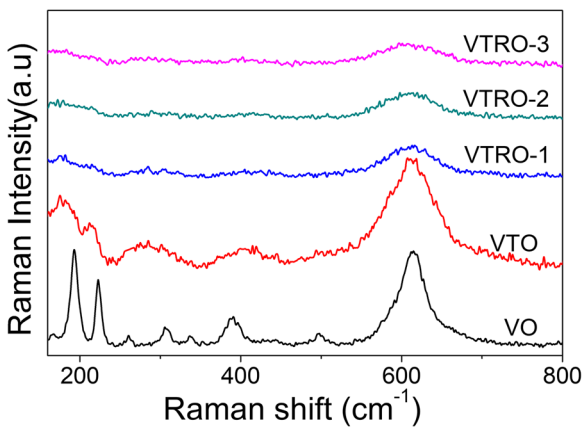

Fig. 4 Room-temperature Raman spectra for undoped VO_2, Ti-doped VO_2 and $V_{1-x-y}Ti_xRu_yO_2$ thin films

Figure 5 shows the SEM surface morphologies for VO, VTO, and VTRO-3. The undoped VO_2 film is mainly composed of particles with size around 50–100 nm (Fig. 5a). Ti-doping obviously influences the surface morphology of VO_2 films. VTO has a bigger particle size than VO (Fig. 5b). This further indicates that Ti-doping facilitates the growth of VO_2 crystallites, which is accordant with the XRD data. Differently, VTRO-3 has a denser and smoother surface morphology than VO and VTO (Fig. 5c), which is preferable for fabricating the high-quality pixels in a mircobolometer. Dense surface morphology of VTRO-3 should originate from the inhibition effect of Ru^{4+} ions in VO_2 lattice on the crystalline growth as revealed by the XRD analysis. Ru^{4+} ions suppress the coalescence of VO_2 grains by restraining the grain boundary (GB) mobility [24]. VTRO-3 has smaller crystallite size than VO and VTO (Table 1). As a result, smaller grains in VTRO-3 constitute denser films than VO and VTO as shown in Fig. 5.

Figure 6 a compares the temperature dependence of resistivity (ρ) for undoped VO_2 film and $V_{1-x-y}Ti_xRu_yO_2$ thin films. VO has a typical SMT feature of polycrystalline VO_2 thin films with a SMT amplitude (ratio of the resistivity at 26 °C to the one at 90 °C) of about 3 orders of magnitude, a hysteresis width of 13.4 °C, and the SMT temperature of 72.1 °C (obtained from the plot dln ρ/dT vs. T in Fig. 6b) [40–42]. Interestingly, Ti-doped thin film (VTO) exhibits no abrupt change of resistivity with temperature from RT to 106 °C (Fig. 6c) although it has the same monoclinic structure at RT as VO. This indicates that the SMT of VO_2 is restrained by Ti-doping with high concentration. The no-SMT feature can avoid the hysteresis and strain changes due to the SMT of VO_2 across the SMT temperature, which is valuable for the application in microbolometers. With further doping with Ru, the no-SMT feature is maintained in $V_{1-x-y}Ti_xRu_yO_2$ thin films (Fig. 6c). Moreover, the resistivity of thin films at RT obviously decreases with the increase of Ru concentration (Table 1). The resistivity at RT of VTRO-3 (1.55 Ω·cm) is only one-eighth of VO (13.5 Ω·cm). Generally, the resistivity of polycrystalline films includes grain resistivity and GB resistivity. The decrease of grain size in films results in the increase of GB density, thus increases resistivity owing to GB scattering [43]. VTRO-3 has smaller grain size than VO as revealed by the SEM analysis (Fig. 5). The GB resistivity in VTRO-3 should be larger than that in VO due to increased GB density. But the predicted change trend of GB resistivity with grain size contradicts the change of film resistivity with doping. Therefore, the grain resistivity, rather than GB one, could play a predominant role

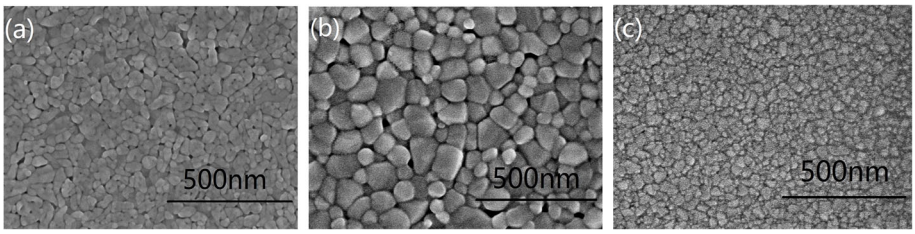

Fig. 5 SEM images of the surface morphologies for **a** VO, **b** VTO, and **c** VTRO-3

in the resistivity of VO_2 polycrystalline thin films. The outstandingly reduced resistivity of VTRO-3 could result from the remarkable decrease of grain resistivity due to the incorporation of Ru^{4+} ions. Substitutional Ru^{4+} ions conduce to induce local tetragonal symmetry in monoclinic VO_2 lattice, which has been demonstrated by previous work [24]. This causes the upward shift of the maximum of valence band and increase of the density of states of the V 3d electrons, which results in the remarkable decrease of grain resistivity. Thus, VTRO-3 exhibits much lower resistivity than VO. Lower resistivity of thermal sensitive materials generally indicates smaller noise and larger electrical magnification for microbolometer devices, thus higher sensitivity of microbolometers [2]. More importantly, VTRO-3 with low resistivity has large TCR (3.47%/°C), similar to undoped VO_2 thin film (VO). It is reasonable since semiconductor VO_2 with monoclinic structure generally exhibits large TCR [44]. As revealed by XRD, Raman, and TEM analyses, $V_{1-x-y}Ti_xRu_yO_2$ thin films have same monoclinic structure as undoped VO_2. So, they retain high TCR as monoclinic VO_2. The TCR value of VTRO-3 is 1.7 times VO_x thin films used in commercial microbolometers (about 2%/°C). This is valuable for increasing the sensitivity of microbolometers since it is proportional to the TCR of thermal-sensitive materials [1]. Therefore, $V_{1-x-y}Ti_xRu_yO_2$ thin film with preferred dopant concentrations (VTRO-3) has attractive characteristics (no-SMT feature, low resistivity, and high TCR) of thermal-sensitive materials for high-performance microbolometers. Furthermore, $V_{1-x-y}Ti_xRu_yO_2$ thin film exhibits superior trade-off performance to other vanadium oxide-based thermal-sensitive thin films as shown in Table 2. This indicates that $V_{1-x-y}Ti_xRu_yO_2$ could be a promising thermal-sensitive material for microbolometers.

In order to investigate the mechanism resulting in the no-SMT feature in Ti-doped VO_2 and $V_{1-x-y}Ti_xRu_yO_2$ thin films, the Raman spectra of VTO and VTRO-3 are acquired at different temperature. As a control, the temperature dependence of the Raman spectrum for undoped VO_2 thin film (VO) is shown in Fig. 7 as well. Considering that the high-frequency mode ω_3 is generally reckoned as a fingerprint for the monoclinic VO_2 [36], the change of this peak with temperature is analyzed. As indicated in Fig. 7a, a clear Raman peak from ω_3 can be observed for VO before the SMT although the integrated Raman intensity decreases from RT to 60 °C. After the SMT, no Raman peak from ω_3 can be probed due to the complete structural transition from monoclinic to tetragonal lattice [39]. Differently, the ω_3 peak can be observed for VTO till 106 °C (Fig. 7b). This indicates the existence of monoclinic VO_2 in VTO from RT to 106 °C. It has reported that Ti-doping increases the SMT temperature of VO_2 for a low doping level [48, 49]. But the SMT temperature saturates at 80–85 °C as the doping level reaches above about 8at% [37, 50]. The previous literature demonstrated the SMT amplitude of Ti-

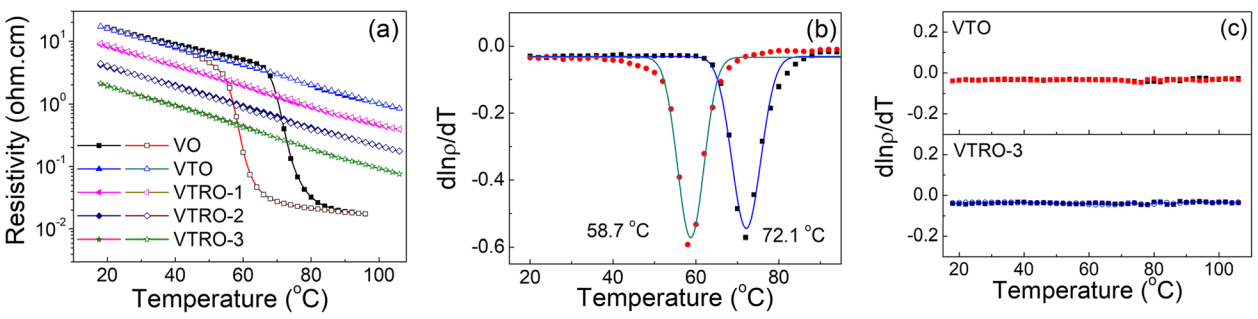

Fig. 6 a Temperature dependence of ρ for all the samples, plots of dln ρ/dT vs. T for **b** VO and **c** VTO and VTRO-3

Table 2 TCR, RT resistivity, and processing temperature of $V_{0.8163}Ti_{0.165}Ru_{0.0187}O_2$ and other vanadium oxide-based thermal-sensitive thin films previously reported

Material	−TCR (%/°C)	Resistivity (Ω·cm)	Processing temperature (°C)	References
VO_x	~ 2.7	2	No heating	[45]
Mo-doped VO_x	4.0–4.5	> 1000	300	3
Mo-doped VO_x	2.5	0.3	No heating	[45]
Nb-doped VO_x	2.1	0.5	No heating	[45]
Ti-doped VO_x	2.5	~ 360	370	[46]
Ta-doped VO_x	3.47	9.32	400	[47]
$V_{0.8163}Ti_{0.165}Ru_{0.0187}O_2$	3.47	1.55	400	This work

doped VO_2 thin films obviously decreases with Ti-doping level, owing to outstanding increase of the resistivity for the metal state [48]. This could originate from stronger Ti–O bonds than V–O ones. It is well-known that the SMT of VO_2 is associated with structural transformation from monoclinic phase to tetragonal phase [51]. Compared with the tetragonal phase, monoclinic VO_2 has remarkably lowered symmetry, which is characterized by zigzag V-V chains with two V-V distances (2.65 and 3.12 Å) [51, 52]. As the temperature rises across the SMT temperature, zigzag V-V chains in the monoclinic phase are transformed into linear V-V chains with a unique V-V distance of about 2.85 Å in the tetragonal phase. Ti has more negative standard heat of formation of oxides than V [53]. This indicates that Ti–O bonds are stabler than V–O bonds. For Ti-doped VO_2, strong Ti–O bonds stabilize the zigzag V-V chains around them due to the pinning effect. This causes some monoclinic domains to be kept in tetragonal lattice across the SMT. As a result, the post-SMT resistivity of Ti-doped VO_2 films obviously increases with Ti-doping level since monoclinic VO_2 has much higher resistivity than tetragonal one. As the concentration of Ti reaches a relatively high value, such as about 17% for VTO, most of monoclinic structures are maintained after the temperature goes above the SMT temperature of VO_2. As a result, monoclinic structure can be detected in VTO till 106 °C (Fig. 7b). Similar mechanism works for $V_{1-x-y}Ti_xRu_yO_2$ thin films since Ti^{4+} ions with equivalent concentration to VTO are doped into VTRO thin films. So, the monoclinic structure can be also observed in VTRO-3 till 106 °C as shown in Fig. 7c. Enhanced

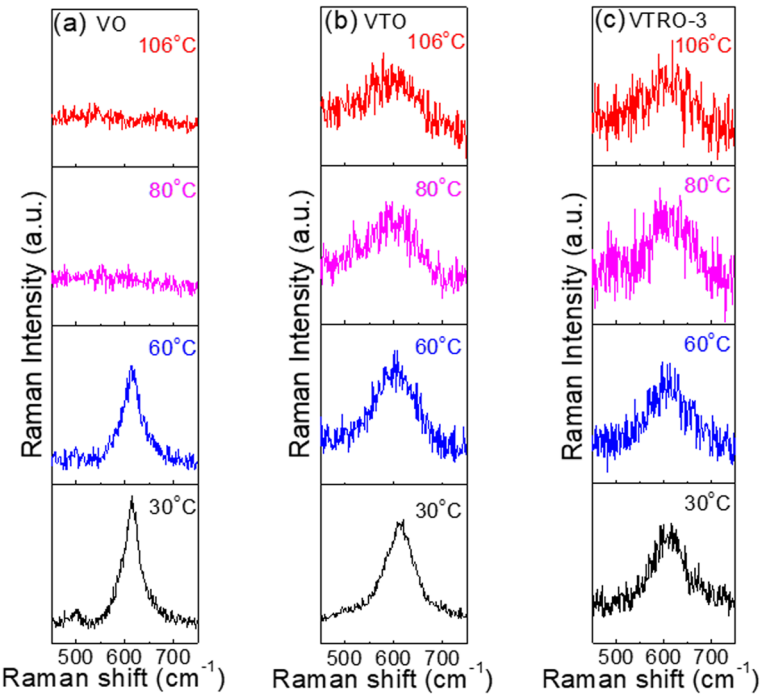

Fig. 7 Temperature-dependent Raman scattering characteristics of **a** VO, **b** VTO, and **c** VTRO-3 during the heating

stability of monoclinic structure causes the no-SMT feature in Ti-doped VO_2 thin film and $V_{1-x-y}Ti_xRu_yO_2$ thin films.

Low RT resistivity of $V_{1-x-y}Ti_xRu_yO_2$ thin films should result from the enhanced local symmetry in monoclinic lattice through the substitutional doping of Ru^{4+} ions [24]. Figure 8 shows the XPS valence band (VB) spectra of VO and VTRO-3. Their VB spectra exhibit a two-region structure, consisting of a broad O 2p band and a V 3d band. The band edge at about 0.3 eV reveals the semiconductor state of undoped VO_2 (VO). Compared with VO, a shift of the V 3d band towards the Fermi level (E_F) can be observed for VTRO-3. Moreover, the ratio of the integrated intensity of the V 3d band to that of the O 2p band for VTRO-3 (6.23%) is larger than that for VO (4.62%). This suggests that the density of states (DOS) of the V3d band for VTRO-3 increases compared with that for VO [24, 54]. According to the Goodenough's model, the zigzag V-V chains in monoclinic VO_2 causes the splitting of the $d_{||}$ band of V 3d electrons into lower and upper $d_{||}$ bands, which results in a bandgap. Thus, monoclinic VO_2 exhibits a semiconductor state [41, 55]. After doping with Ru^{4+} ions, enhanced local symmetry weakens the splitting of the $d_{||}$ band. This leads to the upward shift of the maximum of VB and the increase of the DOS of the V 3d band [24]. So, more electrons can jump at RT from the VB to the conduction band. Therefore, $V_{1-x-y}Ti_xRu_yO_2$ thin films have much lower RT resistivity than undoped one.

Conclusions

$V_{1-x-y}Ti_xRu_yO_2$ thin films have been prepared by a reactively magnetron co-sputtering process followed by annealing at 400 °C. Ru^{4+} and Ti^{4+} ions are incorporated into VO_2 monoclinic lattice by substitution. Although $V_{1-x-y}Ti_xRu_yO_2$ thin films have the same monoclinic structure as undoped VO_2, the co-existence of Ti and Ru ions deceases the crystallite size of films. This results in smoother surface morphology than VO_2 thin films. Ti^{4+} ions in the V-V chains of monoclinic VO_2 stabilize, to some extent, the zigzag V-V chains owing to the pinning effect due to stronger bond strength of Ti–O bonds than V–O bonds. This brings about the no-SMT feature of Ti-doping and Ti-Ru co-doped thin films. $V_{1-x-y}Ti_xRu_yO_2$ thin films with monoclinic structure exhibit large TCR as monoclinic VO_2. Enhanced local symmetry due to the Ru-doping leads to much lower RT resistivity for $V_{1-x-y}Ti_xRu_yO_2$ thin films than undoped one. $V_{1-x-y}Ti_xRu_yO_2$ is one of promising thermal-sensitive materials for fabricating high-performance small-pixel microbolometers.

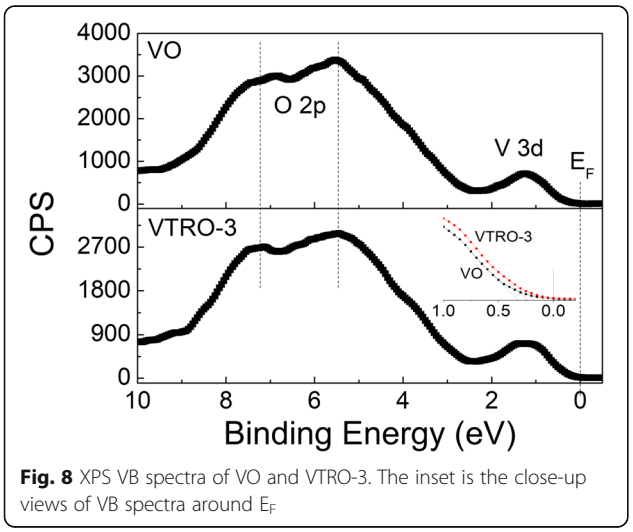

Fig. 8 XPS VB spectra of VO and VTRO-3. The inset is the close-up views of VB spectra around E_F

Abbreviations

SMT: Semiconductor-metal transition; VO_2: Vanadium dioxide; TCR: Temperature coefficient of resistance; RT: Room temperature; MEMS: Micro-electromechanical system; VO_x: Vanadium oxide; DC: Direct current; XPS: X-ray photoelectron spectroscopy; BEs: Binding energies; EDS: Energy dispersive X-ray spectroscopy; XRD: X-ray diffraction; TEM: Transmission electron microscopy; SEM: Scanning electron microscopy; SAD: Selective area diffraction; FFT: Fast Fourier transform

Acknowledgements

The authors gratefully acknowledge the financial support given for this work by the National Natural Science Foundation of China.

Authors' Contributions

YTL prepared the manuscript, and SYX carried out the experiments and collected dat. DEG conceived the idea and designed the experiments. XZ, KY, and YDJ helped in the technical support for the characterizations. All the authors discussed the results and approved the final manuscript.

Funding

This work was supported by the National Natural Science Foundation of China (Grant No. 61841501 and 61421002).

Availability of Data and Materials

All data and materials are fully available without restriction.

Competing Interests

The authors declare that they have no competing interests.

Received: 29 November 2019 Accepted: 13 April 2020
Published online: 22 April 2020

References

1. Rogalski A, Martyniuk P, Kopytko M (2016) Challenges of small-pixel infrared detectors: a review. Rep Prog Phys 4(79):046501 https://doi.org/10.1088/0034-4885/79/4/046501
2. Venkatasubramanian C, Cabarcos OM, Allara DL, Horn MW, Ashok S, Vac J (2009) Correlation of temperature response and structure of annealed VO_x thin films for IR detector applications. J Vac Sci Technol A 4(27):956–961 https://doi.org/10.1116/1.3143667
3. Jin Y, Basantani HA, Ozcelik A, Jackson TN, Horn MW (2013) High resistivity and high TCR vanadium oxide thin films for infrared imaging prepared by bias target ion beam deposition. Proc Spie 8704:87043C https://doi.org/10.1117/12.2016277
4. Yung CS, Tomlin NA, Straatsma C, Rutkowski J, Richard EC (2019) New thermally isolated pixel structure for high-resolution (640 X 480) uncooled infrared focal plane arrays. Opt Eng 1(45):014001 https://doi.org/10.1117/1.2151892
5. Han J-H, Choi J-M, Lee S-H, Jeon W, Park J-S (2018) Chemistry of SiN_x thin film deposited by plasma-enhanced atomic layer deposition using di-isopropylaminosilane (DIPAS) and N_2 plasma. Ceram Int 17(44):20890–20895 https://doi.org/10.1016/j.ceramint.2018.08.095

6. Surana VK, Bhardwaj N, Rawat A, Yadav Y, Ganguly S, Saha D (2019) Realization of high quality silicon nitride deposition at low temperatures. J Appl Phys 17(126):115302 https://doi.org/10.1063/1.5114927
7. Dai J, Wang X, He S, Huang Y, Yi X (2008) Low temperature fabrication of VO_x thin films for uncooled IR detectors by direct current reactive magnetron sputtering method. Infrared Phys Techn 4(51):287–291 https://doi.org/10.1016/j.infrared.2007.12.002
8. Gu D, Zhou X, Guo R, Wang Z, Jiang Y (2017) The microstructures and electrical properties of Y-doped amorphous vanadium oxide thin films. Infrared Phys Techn 81:64–68 https://doi.org/10.1016/j.infrared.2016.12.013
9. Su Y-Y, Cheng X-W, Li J-B, Dou Y-K, Rehman Fida SD-Z, Jin H-B (2015) Evolution of microstructure in vanadium oxide bolometer film during annealing process. Appl Surf Sci 357:887–891 https://doi.org/10.1016/j.ijleo.2015.06.076
10. Loquai S, Baloukas B, Zabeida O, Klemberg-Sapieha JE, Martinu L (2016) HiPIMS-deposited thermochromic VO_2 films on polymeric substrates. Sol Energy Mater Sol Cells 155:60–69 https://doi.org/10.1016/j.solmat.2016.04.048
11. Liu K, Cheng C, Suh J, Tang-Kong R, Fu D, Lee S, Zhou J, Chua LO, Wu J (2014) Powerful, multifunctional torsional micromuscles activated by phase transition. Adv Mater 11(26):1746–1750 https://doi.org/10.1002/adma.201304064
12. Strelcov E, Lilach Y, Kolmakov A (2009) Gas sensor based on metal-insulator transition in VO_2 nanowire thermistor. Nano Lett 6(9):2322–2326 https://doi.org/10.1021/nl900676n
13. Saradha T, Subramania A, Balakrishnan K, Muzhumathi S (2015) Microwave-assisted combustion synthesis of nanocrystalline Sm-doped $La_2Mo_2O_9$ oxide-ion conductors for SOFC application. Mater Res Bull 68:320–325 https://doi.org/10.1016/j.materresbull.2015.03.071
14. Soltani M, Chaker M, Haddad E, Kruzelecky RV, Margot J (2004) Effects of Ti–W codoping on the optical and electrical switching of vanadium dioxide thin films grown by a reactive pulsed laser deposition. Appl Phys Lett 11(85):1958–1960 https://doi.org/10.1063/1.1788883
15. Chaker A, Szkutnik PD, Pointet J, Gonon P, Vallee C, Bsiesy A (2016) Understanding the mechanisms of interfacial reactions during TiO_2 layer growth on RuO_2 by atomic layer deposition with O_2 plasma or H_2O as oxygen source. J Appl Phys 8(120):085315 https://doi.org/10.1063/1.4960139
16. Yue H, Xue L, Chen F (2017) Efficiently electrochemical removal of nitrite contamination with stable RuO_2–TiO_2/Ti electrodes. Appl Catal B 206:683–691 https://doi.org/10.1016/j.apcatb.2017.02.005
17. Ji C, Wu Z, Lu L, Wu X, Wang J, Liu X, Zhou H, Huang Z, Gou J, Jiang Y (2018) High thermochromic performance of Fe/Mg co-doped VO_2 thin films for smart window applications. J Mater Chem C 24(6):6502–6509 https://doi.org/10.1039/c8tc0111g
18. Shi Q, Huang W, Wu J, Zhang Y, Xu Y, Zhang Y, Qiao S, Yan J (2012) Terahertz transmission characteristics across the phase transition in VO_2 films deposited on Si, sapphire, and SiO_2 substrates. J Appl Phys 3(112):033523 https://doi.org/10.1063/1.4746701
19. Shi Q, Huang W, Zhang Y, Yan J, Zhang Y, Mao M, Zhang Y, Tu M (2011) Giant phase transition properties at terahertz range in VO_2 films deposited by sol-gel method. ACS Appl Mater Interface 9(3):3523–3527 https://doi.org/10.1021/am200734k
20. Zhang H, Wu Z, Niu R, Wu X, He Q, Jiang Y (2015) Metal–insulator transition properties of sputtered silicon-doped and un-doped vanadium dioxide films at terahertz range. Appl Surf Sci 331:92–97 https://doi.org/10.1016/j.apsusc.2015.01.013
21. Zhang Z, Gao Y, Chen Z, Du J, Cao C, Kang L, Luo H (2010) Thermochromic VO_2 thin films: solution-based processing, improved optical properties, and lowered phase transformation temperature. Langmuir 13(26):10738–10744 https://doi.org/10.1021/la100515k
22. Li B, Tian S, Tao H, Zhao X (2019) Tungsten doped M-phase VO_2 mesoporous nanocrystals with enhanced comprehensive thermochromic properties for smart windows. Ceram Int 4(45):4342–4350 https://doi.org/10.1016/j.ceramint.2018.11.109
23. Zhang Y, Zhang J, Zhang X, Huang C, Zhong Y, Deng Y (2013) The additives W, Mo, Sn and Fe for promoting the formation of VO_2(M) and its optical switching properties. Mater Lett 92:61–64 https://doi.org/10.1016/j.matlet.2012.10.054
24. Gu D, Zheng H, Ma Y, Xu S, Zhou X (2019) A highly-efficient approach for reducing phase transition temperature of VO_2 polycrystalline thin films through Ru^{4+} -doping. J Alloy Compd 790:602–609 https://doi.org/10.1016/j.jallcom.2019.03.214
25. Wang M, Bian J, Sun H, Liu W, Zhang Y, Luo Y (2016) n-VO_2/p-GaN based nitride–oxide heterostructure with various thickness of VO_2 layer grown by MBE. Appl Surf Sci (389):199–204 https://doi.org/10.1016/j.apsusc.2016.07.109
26. Bian J, Wang M, Miao L, Li X, Luo Y, Zhang D, Zhang Y (2015) Growth and characterization of VO_2/p-GaN/sapphire heterostructure with phase transition properties. Appl Surf Sci 357:282–286 https://doi.org/10.1016/j.apsusc.2015.08.263
27. Li D, Li M, Pan J, Luo Y, Wu H, Zhang Y, Li G (2014) Hydrothermal synthesis of Mo-doped VO_2/TiO_2 composite nanocrystals with enhanced thermochromic performance. ACS Appl Mater Interface 9(6):6555–6561 https://doi.org/10.1021/am500135d
28. Chen S, Liu J, Wang L, Luo H, Gao Y (2014) Unraveling mechanism on reducing thermal hysteresis width of VO_2 by Ti doping: a joint experimental and theoretical study. J Phys Chem C 33(118):18938–18944 https://doi.org/10.1021/jp5056842
29. Nishikawa M, Nakajima T, Kumagai T, Okutani T, Tsuchiya T (2011) Ti-doped VO_2 films grown on glass substrates by excimer-laser-assisted metal organic deposition process. Jpn J Appl Phys 1(50): 01BE04 https://doi.org /10.1143/JJAP.50.01BE04
30. Balamurugan C, Maheswari AR, Lee DW, Subramania A (2013) Selective ethanol gas sensing behavior of mesoporous n-type semiconducting $FeNbO_4$ nanopowder obtained by niobium–citrate process. Curr Appl Phys 14:439–446 https://doi.org/10.1016/j.cap.2013.11.052
31. Balamurugan C, Subashini A, Chaudhari GN, Subramania A (2012) Development of wide band gap sensor based on $AlNbO_4$ nanopowder for ethanol. J Alloy Compd 526:110–115 http://dx.doi.org/. https://doi.org/10.1016/j.jallcom.2012.01.085
32. Guo M, Xia X, Gao Y, Jiang G, Deng Q, Shao G (2012) Self-aligned TiO_2 thin films with remarkable hydrogen sensing functionality. Sens Actuators B 168:165–171 https://doi.org/10.1016/j.snb.2012.02.072
33. Balamurugan C, Vijayakumar E, Subramania A (2012) Synthesis and characterization of $InNbO_4$ nanopowder for gas sensors. Talanta 88:115–120 https://doi.org/10.1016/j.talanta.2011.10.017
34. Gu D, Li Y, Zhou X, Xu Y (2019) Facile fabrication of composite vanadium oxide thin films with enhanced thermochromic properties. ACS Appl Mater Interface 41(11):37617–37625 https://doi.org/10.1021/acsami.9b11376
35. Urena-Begara F, Crunteanu A, Raskin JP (2017) Raman and XPS characterization of vanadium oxide thin films with temperature. Appl Surf Sci 403:717–727 https://doi.org/10.1016/j.apsusc.2017.01.160
36. Okimura K, Azhan NH, Hajiri T, Kimura S, Zaghrioui M, Sakai J (2014) Temperature-dependent Raman and ultraviolet photoelectron spectroscopy studies on phase transition behavior of VO_2 films with M1 and M2 phases. J Appl Phys 15(115):153501 https://doi.org/10.1063/1.4870868
37. Du J, Gao Y, Luo H, Kang L, Zhang Z, Chen Z, Cao C (2011) Significant changes in phase-transition hysteresis for Ti-doped VO_2 films prepared by polymer-assisted deposition. Sol Energy Mater Sol Cells 2(95):469–475 https://doi.org/10.1016/j.solmat.2010.08.035
38. Aetukuri NB, Gray AX, Drouard M, Cossale M, Gao L, Reid AX, Kukreja R, Ohldag H, Jenkins CA, Arenholz E, Roche KP, Dürr HA, Samant MG, Parkin SSP (2013) Control of the metale-insulator transition in vanadium dioxide by modifying orbital occupancy. Nat Phys 10(9):661–666 https://www.nature.com/articles/nphys2733
39. Whittaker L, Wu T, Stabile A, Sambandamurthy G, Banerjee S (2011) Single-nanowire Raman microprobe studies of doping-, temperature-, and voltage-induced metal-insulator transitions of $W_xV_{1-x}O_2$ nanowires. ACS Nano 11(5):8861–8867 https://doi.org/10.1021/nn203542c
40. Gu D, Sun Z, Zhou X, Guo R, Wang T, Jiang Y (2015) Effect of yttrium-doping on the microstructures and semiconductor-metal phase transition characteristics of polycrystalline VO_2 thin films. Appl Surf Sci 359:819–825 https://doi.org/10.1016/j.apsusc.2015.10.179
41. Gu D, Zhou X, Sun Z, Jiang Y (2017) Influence of Gadolinium-doping on the microstructures and phase transition characteristics of VO_2 thin films. J Alloy Compd 705:64–69 https://doi.org/10.1016/j.jallcom.2017.02.138
42. Zhang R, Yin C, Fu Q, Li C, Qian G, Chen X (2018) Metal-to-insulator transition and its effective manipulation studied from investigations in $V_{1-x}Nb_xO_2$ bulks. Ceram Int 3(44):2809–2813 https://doi.org/10.1016/j.ceramint.2017.11.024
43. Wu W, Brongersma SH, Van Hove M, Maex K (2004) Influence of surface and grain-boundary scattering on the resistivity of copper in reduced dimensions. Appl Phys Lett 15(84):2838–2840 https://doi.org/10.1063/1.1703844

44. Chen X, Lv Q (2015) Resistance hysteresis loop characteristic analysis of VO_2 thin film for high sensitive microbolometer. Optik 20(126):2718–2722 https://doi.org/10.1016/j.ijleo.2015.06.076
45. Ozcelik A, Cabarcos O, Allara DL, Horn MW (2013) Vanadium oxide thin films alloyed with Ti, Zr, Nb, and Mo for uncooled infrared imaging applications. J Electron Mater 5(42):901–905 https://doi.org/10.1007/s11664-012-2326-9
46. Wang S, Yu S, Lu M, Liu M, Zuo L (2017) Atomic layer-deposited titanium-doped vanadium oxide thin films and their thermistor applications. J Electron Mater 4(46):2153–2157 https://doi.org/10.1007/s11664-016-5150-9
47. Lee H-Y, Wu C-L, Kao C-H, Lee C-T, Tang S-F, Lin W-J, Chen H-C, Lin J-C (2015) Investigated performance of uncooled tantalum-doped VO_x floating-type microbolometers. Appl Surf Sci 354:106–109 https://doi.org/10.1016/j.apsusc.2015.03.008
48. Huang K, Meng Y, Xu X, Chen P, Lu A, Li H, Wu B, Wang C, Chen X (2017) Orbital electronic occupation effect on metal–insulator transition in $Ti_xV_{1-x}O_2$. J Phys: Condens Matter 35(29):355402 https://doi.org/10.1088/1361-648X/aa7707
49. Hu Y, Shi Q, Huang W, Zhu H, Yue F, Xiao Y, Liang S, Lu T (2016) Preparation and phase transition properties of Ti-doped VO_2 films by sol–gel process. J Sol-Gel Sci Technol 1(78):19–25 https://doi.org/10.1007/s10971-015-3913-z
50. Wu Y, Fan L, Liu Q, Chen S, Huang W, Chen F, Liao G, Zou C, Wu Z (2015) Decoupling the lattice distortion and charge doping effects on the phase transition behavior of VO_2 by Ti^{4+} doping. Sol Energy Mater Sol Cells 5:9328 https://doi.org/10.1038/srep09328
51. Whittaker L, Patridge CJ, Banerjee S (2011) Microscopic and nanoscale perspective of the metal insulator phase transitions of VO_2 some new twists to an old tale. J Phys Chem Lett 7(2):745–758 https://doi.org/10.1021/jz101640n
52. Gupta SN, Pal A, Muthu DVS, Anil Kumar PS, Sood AK (2016) Metallic monoclinic phase in VO_2 induced by electrochemical gating: in situ Raman study. EPL 1(115):17001 https://doi.org/10.1209/0295-5075/115/17001
53. Campbell CT (1997) Ultrathin metal films and particles on oxide surfaces: structural, electronic and chemisorptive properties. Surf Sci Rep 1-3(27):1–111 https://doi.org/10.1016/S0167-5729(96)00011-8
54. Muraoka Y, Nagao H, Katayama S, Wakita T, Hirai M, Yokoya T, Kumigashira H, Oshima M (2014) Persistent insulator-to-metal transition of a VO_2 thin film induced by soft X-ray irradiation. Jpn J Appl Phys 5(53):05FB09 https://doi.org/10.7567/JJAP.53.05FB09
55. Goodenough JB (1971) Anomalous properties of the vanadium oxides. Annu Rev Mater Sci 1:101–138 https://www.annualreviews.org/doi/10.1146/annurev.ms.01.080171.000533

Publisher's Note